nature communications

Article

https://doi.org/10.1038/s41467-024-54589-0

Operando elucidation of hydrogen production mechanisms on sub-nanometric high-entropy metallenes

Received: 1 December 2023

Accepted: 15 November 2024

Published online: 25 November 2024

Check for updates

Yinghao Li[1,6], Chun-Kuo Peng[2,3,6], Yuntong Sun[1] ✉, L. D. Nicole Sui[1,4], Yu-Chung Chang[3], San-Yuan Chen[2], Yingtang Zhou[5] ✉, Yan-Gu Lin[2,3] ✉ & Jong-Min Lee[1] ✉

Precise morphological control and identification of structure-property relationships pose formidable challenges for high-entropy alloys, severely limiting their rational design and application in multistep and tandem reactions. Herein, we report the synthesis of sub-nanometric high-entropy metallenes with up to eight metallic elements via a one-pot wet-chemical approach. The PdRhMoFeMn high-entropy metallenes exhibit high electrocatalytic hydrogen evolution performances with 6, 23, and 26 mV overpotentials at −10 mA cm^{-2} in acidic, neutral, and alkaline media, respectively, and high stability. The electrochemical measurements, theoretical simulations, and operando X-ray absorption spectroscopy reveal the actual active sites along with their dynamics and synergistic mechanisms in various electrolytes. Specially, Mn sites have strong binding affinity to hydroxyl groups, which enhances the water dissociation process at Pd sites with low energy barrier while Rh sites with optimal hydrogen adsorption free energy accelerate hydride coupling, thereby markedly boosting its intrinsic ability for hydrogen production.

Electrochemical hydrogen evolution reaction (HER) is an eco-friendly, cost-efficient, and feed-rich technology to manufacture high gravimetric-energy-density and clean hydrogen fuels, which can satisfy rising energy demand while mitigating environmental situations by efficiently converting and storing electricity from intermittent sources (e.g., wind or solar) in their chemical form[1–5]. Hitherto, Pt-based nanomaterials are the most sophisticated HER electrocatalysts owing to their first-rank bonding strength with hydrogen[6–8]. However, the high cost, suboptimum electrochemical durability, and significantly lower activity in non-acidic electrolytes of Pt bring about tremendous barriers to their large-scale application in electrolyzers and fuel cells[9–11]. This poses a challenge for researchers stemming from the ever-increasing demand for pH-universal HER electrocatalysts with high performance.

High-entropy alloys (HEAs), with five or more elements in near equiatomic ratios and homogeneously mixed solid-solution phase, have excited rapidly growing interest in diverse research areas owing to high configuration entropy, sluggish diffusion, lattice distortion, and cocktail effects[12,13]. Notably, compared with single or bimetallic catalysts, the multi-component adjustability of HEAs can provide different desired active sites and an almost continuous distribution of binding energy to synchronously stabilize all intermediates during

[1]School of Chemistry, Chemical Engineering and Biotechnology, Nanyang Technological University, 62 Nanyang Drive, Singapore 637459, Singapore. [2]Department of Material Science and Engineering, National Yang Ming Chiao Tung University, Hsinchu 300093, Taiwan. [3]Scientific Research Division, National Synchrotron Radiation Research Center, Hsinchu 300092, Taiwan. [4]Environmental Chemistry and Materials Centre, Nanyang Environment & Water Research Institute (NEWRI), Interdisciplinary Graduate Programme, Nanyang Technological University, Singapore 637141, Singapore. [5]Zhejiang Key Laboratory of Petrochemical Environmental Pollution Control, Marine Science and Technology College, Zhejiang Ocean University, Zhoushan 316004, China. [6]These authors contributed equally: Yinghao Li, Chun-Kuo Peng. ✉e-mail: yuntong.sun@ntu.edu.sg; zhouyingtang@zjou.edu.cn; lin.yg@nsrrc.org.tw; jmlee@ntu.edu.sg

multistep catalytic reactions[14]. Meanwhile, particular high-entropy mixing states and sluggish diffusion effect can endow the catalyst with remarkable stability by suppressing the galvanic corrosion and preventing the dissolution of atoms into corrosive electrolytes[15,16]. Similarly, the development of single-atom to high-entropy single-atom catalysts (HESACs) is to impart a variety of different adsorption sites while possessing near 100% utilization efficiency of metal atoms, which is highly beneficial for multistep tandem reactions or reactions requiring multifunctional catalysts (Fig. 1a)[17–20]. However, as for HESACs, the lack of synergistic effects between adjacent metal atoms resulting from fully isolated active sites and over-rigid local constructions limit their activities in specific catalytic reactions like low-temperature carbon monoxide oxidation[21]. Such a tendency will evolve into a definitive scenery of metal elements at the sub-nanometric restriction (nearly 1 nm thickness). Thereinto, sub-nanometric two-dimensional (2D) materials have an extremely large proportion of surface atoms that are accessible to catalytic reactions, which can maximize the utilization efficiency of metal atoms, especially for platinum group metals (PGMs)[22–24]. Meanwhile, high-density active sites show a synergistic effect with neighboring metal atoms, which optimizes their electronic configurations and intermediate adsorption energies, thus boosting their catalytic performance[25–27]. Lamentedly, different metallic elements differ in size, crystal configuration, and electronegativity, resulting in varying degrees of lattice mismatch between them, which is not conducive to HEA formation. Therefore, most of the reported HEAs are still confined to nanoparticles, and the construction of sub-nanometric 2D HEA materials is scarce and challenging[28]. In addition, the applied potential, reaction temperature, or erosive electrolyte leads to the structural transformation or profound reorganization of electrocatalysts during the actual catalytic process, severely hindering the precise identification of the true catalytically active center and the establishment of structure-activity relationships[29]. Recently, operando characterization techniques, such as operando X-ray absorption spectroscopy (XAS), Fourier transform infrared (FTIR) spectroscopy, and Raman spectroscopy, provide an effective way to break these barriers, which can track the kinetics of catalysts and monitor the adsorption/desorption behavior of reactive intermediates during catalysis[30–33] (Supplementary Fig. 1). Nevertheless, most of these techniques are applied to the analysis of single-atom and bimetallic catalytic reaction systems due to their clear and well-defined coordination structures[34–38]. As an equally crucial catalyst system, it remains to be explored to gain atomistic-level insight into active site dynamics and interaction mechanisms for HEAs with tanglesome atomic arrangements and multiple elements of similar electron contrasts under realistic catalytic conditions[39].

This work proposes a general one-pot wet-chemical strategy to fabricate a series of sub-nanometric high-entropy metallenes (HEMs), including but not limited to quinary PdRhMoFeMn, senary PdRhIrCoFeMo, septenary PdRhIrFeMoMnW and octonary PdRhIrMnMoRuFeCo HEMs. The representative quinary PdRhMoFeMn HEMs demonstrate small overpotentials at −10 mA cm^{-2} (η_{10}), high mass activities, and superior stability over a broad pH range (0–14). Density functional theory (DFT) calculations speculate that the Rh site is the possible active center with the optimal hydrogen adsorption free energy (ΔG_{H^*}) (−0.132 eV) in an acidic environment. In neutral and alkaline electrolytes, the Pd site with strong water adsorption energy (−0.34 eV) and small water dissociation energy barrier (0.53 eV) facilitates the dissociation of water to produce protons, followed by the hydrogen spillover from Pd to Rh sites. Additionally, the Mn site shows strong binding energy (−3.05 eV) for hydroxyl groups, which accelerates the water dissociation step. In particular, operando XAS further traces the dynamics of real active sites and visually reveals multi-site synergistic mechanisms for PdRhMoFeMn HEMs in different electrolytes during the electrocatalytic HER, which paves an avenue to rationally design next-generation high-efficiency HEA electrocatalysts with desirable multifunctional active sites for complex multi-electron catalytic processes.

Results

Materials synthesis and characterization

Typical sub-nanometric PdRhMoFeMn HEMs were synthesized via a simple one-pot wet-chemical strategy through heating a mixed solution containing palladium(II) acetylacetonate ($Pd(acac)_2$), hexarhodium hexadecacarbonyl ($Rh_6(CO)_{16}$), dodecacarbonyltriiron ($Fe_3(CO)_{12}$), manganese carbonyl ($Mn_2(CO)_{10}$), molybdenum hexacarbonyl ($Mo(CO)_6$), ascorbic acid (AA), and oleylamine (Supplementary Fig. 2). Low-magnification high-angle annular dark-field scanning transmission electron microscopy (HAADF-STEM) and TEM images in Fig. 1b and Supplementary Fig. 3 show that the obtained products are dominated by graphene-like 2D nanosheets with abundant porous nanochannels. High-resolution TEM (HRTEM) image confirms that PdRhMoFeMn HEMs are ultrathin and possess a certain curvature (Fig. 1c). The thickness of PdRhMoFeMn HEMs was determined to be six atomic layers from the edge seen in aberration-corrected HAADF-STEM (Fig. 1d), in good conformity with a thickness of ~1 nm characterized by AFM atomic force microscopy (AFM), affirming the successful formation of sub-nanometric metallenes (Supplementary Fig. 4). The clear lattice fringes in Fig. 1d indicate a lattice spacing of 0.228 nm, slightly higher than the lattice distance of the Pd (111) facet. Additionally, the X-ray diffraction (XRD) pattern in Fig. 1e shows that PdRhMoFeMn HEMs possess a face-centered cubic (*fcc*) configuration without phase segregation, which is analogous to that of pure Pd. The weakening and broadening of XRD peaks could be attributable to the lattice distortion originating from the interposition of Mn, Fe, Rh, and Mo atoms. The Pd/Rh/Mo/Fe/Mn ratio was determined by the SEM energy dispersive X-ray spectroscopy (SEM-EDS) to be 23.52/20.97/17.42/16.58/21.51 (Fig. 1f). Similar results were obtained from the inductively coupled plasma optical emission spectroscopy (ICP-OES) measurement (Pd/Rh/Mo/Fe/Mn=23.37/19.53/18.07/17.35/21.68) (Supplementary Table 1). The difference between the initial feed ratio and the ratio of elements in the obtained HEMs is due to the difference in the reduction difficulty of various metal precursors[40,41]. Aberration-corrected HAADF-STEM measurements were employed to further analyze the fine structure of PdRhMoFeMn HEMs. As presented in Fig. 1g, h, many lattice distortions including edge dislocation (ED) and stacking fault (SF) are clearly observed in HEMs, which is a fundamental characteristic of high-entropy structures caused by the disordered distribution of atoms on the equivalent sites but with different size, mass, and electronegativity. The lattice distortion feature was further verified by the (111) lattices from different selected regions in PdRhMoFeMn HEMs, where the average lattice distance varies from 0.221 nm (h_4) to 0.229 nm (h_1) to 0.232 nm (h_2) and to 0.239 nm (h_3) (Supplementary Fig. 5). These lattice defects could offer rich low-coordination sites to boost the catalytic activity. Furthermore, aberration-corrected HAADF-STEM-EDS elemental mappings show the homogenous distribution of all elements throughout the HEMs (Fig. 1i). Such a highly stable sub-nanometric HEA nanosheet has been long sought since it can provide various active sites to favor intermediate reaction processes and expose nearly all metal atoms to electrocatalysis, as will be discussed later.

The XAS was performed to deeply probe into the atomic-coordination environment and electronic configuration of sub-nanometric PdRhMoFeMn HEMs. As shown in Fig. 2a, c, the X-ray absorption near-edge structure (XANES) spectra exhibit that the white line intensities of Pd and Rh in PdRhMoFeMn HEMs are closer to Pd and Rh foils and far away from the PdO and Rh_2O_3 reference samples, indicating that the Pd and Rh species in HEMs mainly sit in the metallic state. Compared to the corresponding metal foils, the post-edges of Pd and Rh in HEMs show slight differences in shape and intensity, confirming the establishment of alloys instead of elemental segregation

https://doi.org/10.1038/s41467-024-54589-0

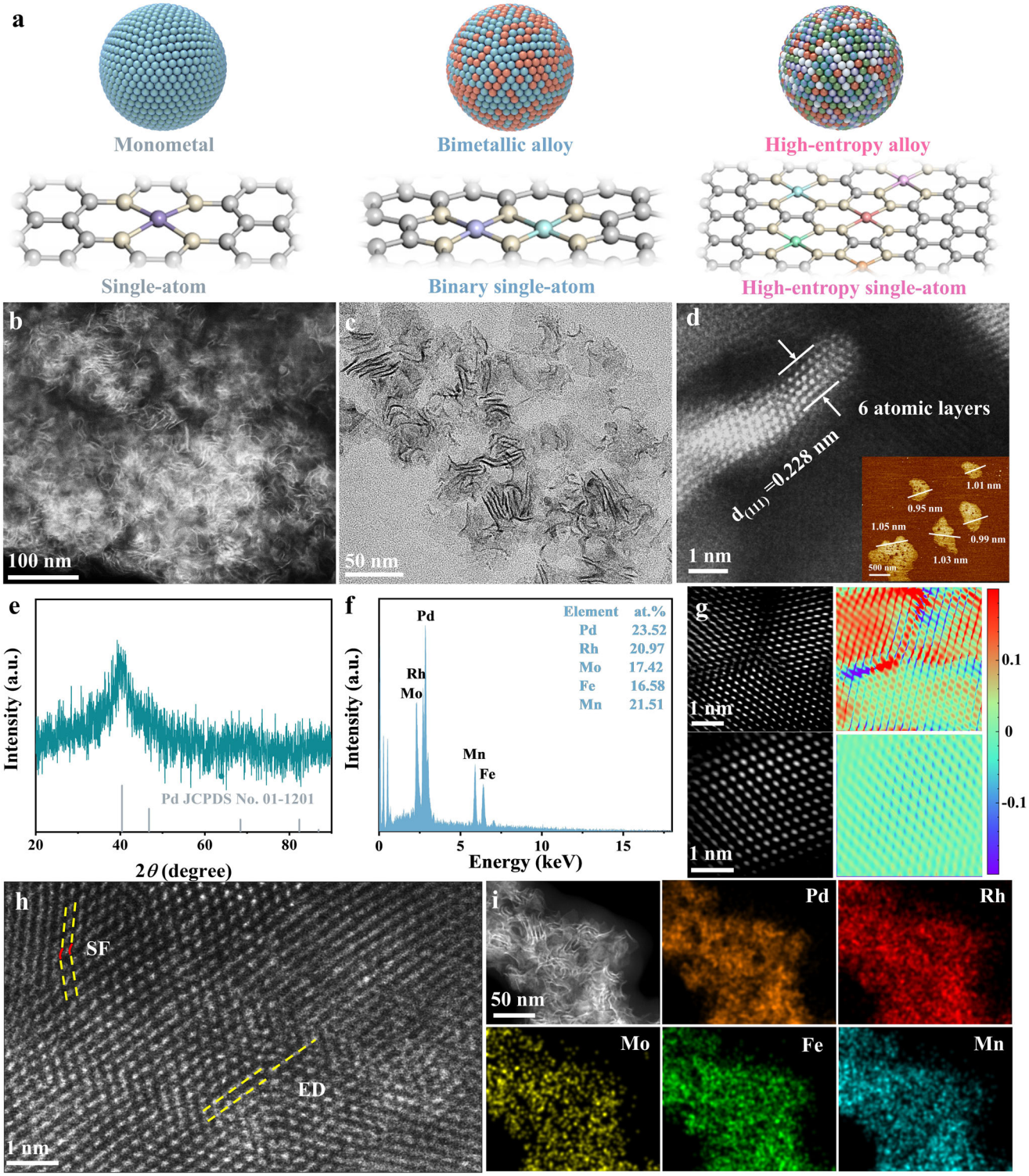

Fig. 1 | Morphology and structure characterizations of sub-nanometric PdRhMoFeMn HEMs. a The structural evolution from monometal catalysts to HEAs and from SACs to HESACs. **b**–**d** Low-resolution HAADF-STEM image (**b**), HRTEM image (**c**), and aberration-corrected HRSTEM image at the edge of a wrinkle (**d**) of PdRhMoFeMn HEMs. The inset in **d** is the AFM image of PdRhMoFeMn HEMs. **e**, **f** XRD (**e**) and SEM-EDS (**f**) results of PdRhMoFeMn HEMs. **g** Aberration-corrected HRSTEM and geometric phase analysis (GPA) images of PdRhMoFeMn HEMs and Pd metallenes. **h**, **i** aberration-corrected HRSTEM (**h**) and EDS elemental mapping images (**i**) of PdRhMoFeMn HEMs.

into pure metals. In addition, the extended X-ray absorption fine structure (EXAFS) spectra of HEMs show an obvious prominent peak at ~2.75 Å for Pd-M (Fig. 2b) and ~2.75 Å for Rh-M (Fig. 2d), respectively. Due to the thinness of the material, lower coordination numbers, and a homogeneous distribution of metal atoms, it is indeed possible to observe Rh-Rh and Pd-Pd neighbors[42,43]. Moreover, Pd-M and Rh-M are slightly distinct from the Pd-Pd and Rh-Rh bonds in Pd and Rh references. This phenomenon results from small changes in the coordination environment caused by the presence of other smaller atoms (Mo, Fe, and Mn) around the relatively large Pd and Rh atoms. Therefore, M

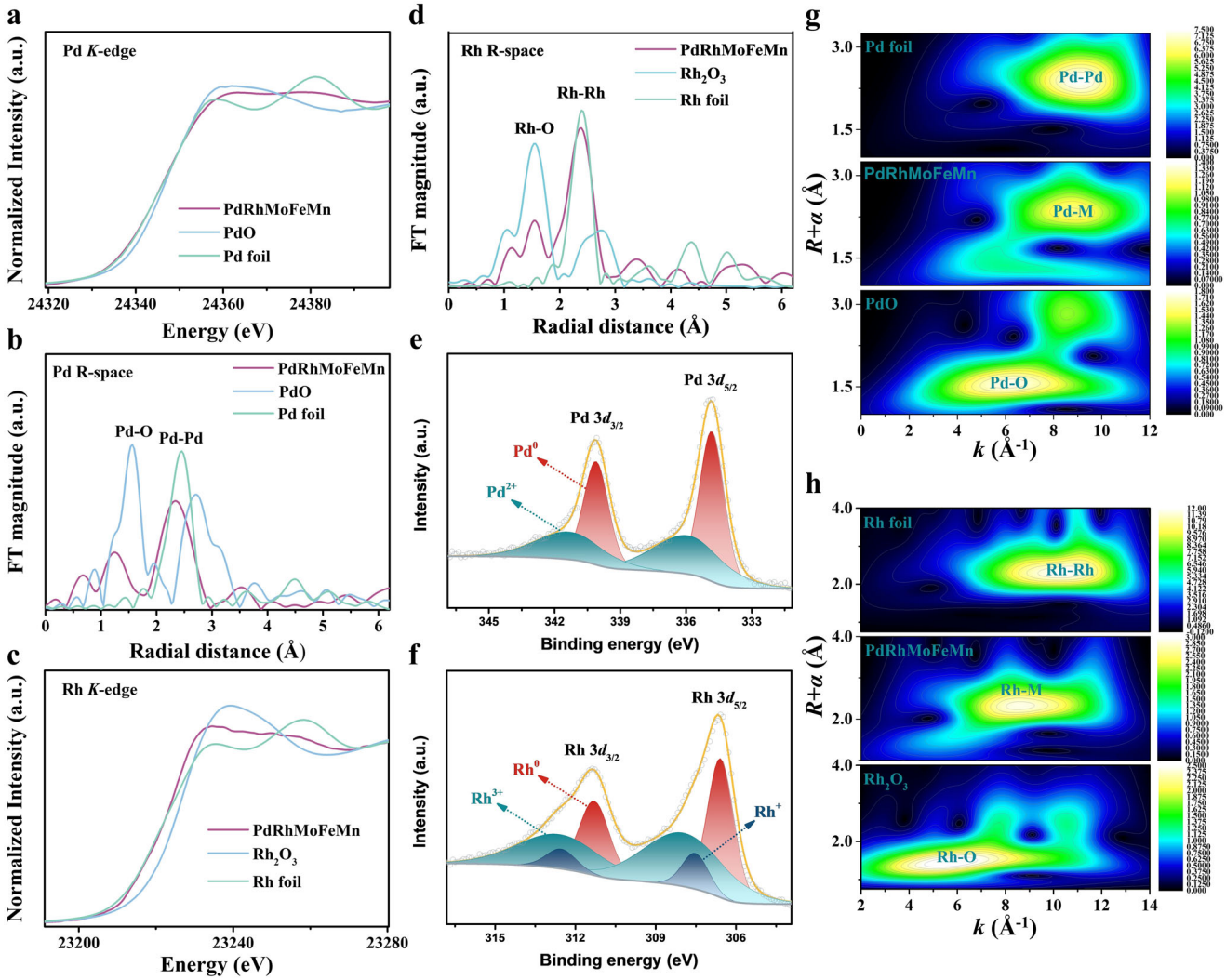

Fig. 2 | Electronic structure investigations. a, **b** The Pd *K*-edge XANES spectra and FT-EXAFS spectra of PdRhMoFeMn HEMs, PdO, and Pd foil with phase correction. **c**, **d** The Rh *K*-edge XANES spectra and FT-EXAFS spectra of PdRhMoFeMn HEMs, Rh_2O_3, and Rh foil with phase correction. **e**, **f** Pd 3 *d* and Rh 3 *d* XPS spectra of PdRhMoFeMn HEMs. **g** 2D WT-EXAFS spectra of PdRhMoFeMn HEMs, PdO, and Pd foil. **h** 2D WT-EXAFS spectra of PdRhMoFeMn HEMs, Rh_2O_3, and Rh foil.

can be Pd, Rh, Mo, Fe, or Mn. The maximum peak intensity of Pd-M and Rh-M at around 8.8 Å can be observed in the wavelength-transformed EXAFS (WT-EXAFS) patterns of Rh and Pd in PdRhMoFeMn HEMs, further verifying a variation in the atomic-coordination environment relative to Pd and Rh foils (Fig. 2g, h). Furthermore, the XANES spectra of Fe, Mo, and Mn show positive energy shifts, suggesting that their chemical states lie between those of the metallic and oxide standard samples, probably due to the exposure of the more easily oxidizable Fe, Mn, and Mo atoms on the catalyst surface (Supplementary Fig. 6). The surface chemical composition of PdRhMoFeMn HEMs was further investigated with X-ray photoelectron spectroscopy (XPS)[44–46]. The XPS survey spectrum identifies that Pd, Rh, Mo, Fe, and Mn elements coexist in HEMs (Supplementary Fig. 7a). The Pd 3*d* XPS spectrum reveals the presence of main metallic Pd and a small amount of palladium oxide, in which the peaks at 334.83 and 340.14 eV correlate to Pd^0 $3d_{5/2}$ and Pd^0 $3d_{3/2}$, respectively (Fig. 2e)[47]. The peaks at 336.08 and 341.47eV match Pd^{2+} $3d_{5/2}$ and Pd^{2+} $3d_{3/2}$[48]. Similarly, the majority of Rh exists as a zero-valence substance, with a small proportion as a 1+ or 3+ substance (Fig. 2f). In detail, the high-resolution Rh 3*d* spectra of PdRhMoFeMn HEMs are composed of six fitting peaks of Rh^0 $3d_{5/2}$ (306.59 eV), Rh^0 $3d_{3/2}$ (311.31 eV), Rh^+ $3d_{5/2}$ (307.54 eV), Rh^+ $3d_{3/2}$ (312.58 eV), Rh^{3+} $3d_{5/2}$ (308.13 eV) and Rh^{3+} $3d_{3/2}$ (312.86 eV)[49]. Furthermore, the Fe 2*p*, Mn 2*p*, and Mo 3*d* spectra indicate that Fe, Mn, and Mo atoms in PdRhMoFeMn HEMs exist in partially oxidized states, consistent with the above-mentioned XANES analysis (Supplementary Fig. 7b–d). Due to the exposure of under-coordinated corner atoms and edge atoms with stronger oxyphilic nature in ultrathin HEMs to air, the trace metal-oxygen species on the catalyst surface are formed, which is a common phenomenon in the reported literature[16,26,50]. Specifically, the HER activity of RhO_2 and PdO is much lower than that of PdRhMoFeMn HEMs (Supplementary Fig. 8), which indicates the effects of these trace amounts of metal-oxygen species on the HER mechanism and performance are minimal, which are generally ignorable in reported literature[42,51,52].

To understand the growth mechanism of PdRhMoFeMn HEMs, time-dependent TEM-EDS experiments were carried out. As demonstrated in Supplementary Fig. 9, $Pd(acac)_2$ is first reduced to form small Pd metallene seeds due to only the appearance of the Pd peak at the first 1 min reaction, then Rh atoms from the decomposition of $Rh_6(CO)_{16}$ begin to integrate into the initial Pd metallene. Finally, Mo, Fe, and Mn atoms decomposed from $Fe_3(CO)_{12}$, $Mn_2(CO)_{10}$, and $Mo(CO)_6$ are alloyed into this nanosheet to form HEMs with a distinctively curved geometry. CO molecules decomposed from carbonyl metal compounds act as a capping agent, confining the Pd (111)-facet growth and leading to the 2D construction, analogous to reported PdMo bimetallene[26]. Using the same preparation scheme but altering

https://doi.org/10.1038/s41467-024-54589-0

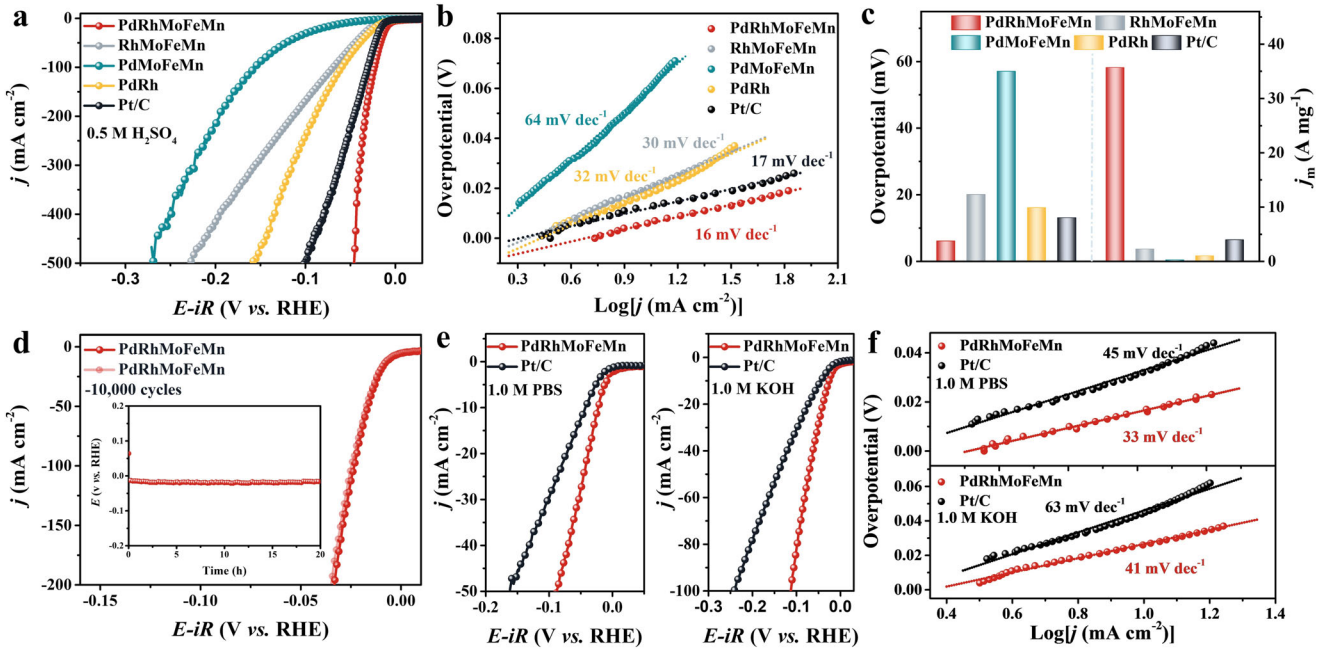

Fig. 3 | Electrocatalytic HER performance evaluation of sub-nanometric PdRhMoFeMn HEMs. The non-iR corrected polarization curves were provided in the Supplementary Information. **a**, **b** Polarization curves with iR-compensation (**a**), corresponding Tafel plots (**b**) of PdRhMoFeMn HEMs, RhMoFeMn metallenes, PdMoFeMn metallenes, PdRh metallenes, and Pt/C in 0.5 M H_2SO_4 electrolyte. **c** η_{10} (left) and mass activities (right) at an overpotential of 50 mV of these nanocatalysts in 0.5 M H_2SO_4 electrolyte. **d** Polarization curves of PdRhMoFeMn HEMs with iR-compensation before and after 10,000 CV cycles in 0.5 M H_2SO_4 electrolyte. The insert is the chronopotentiometry curve of PdRhMoFeMn HEMs without iR-compensation operated at 10 mA cm^{-2} in 0.5 M H_2SO_4 electrolyte. **e**, **f** Polarization curves with iR-compensation (**e**), corresponding Tafel plots (**f**) of PdRhMoFeMn HEMs and Pt/C in 1.0 M PBS and 1.0 M KOH electrolytes, respectively. The testing conditions include GCE surface area: 0.07 cm^2, catalyst loading: 0.286 mg cm^{-2}, nobel metal loading: 0.028 mg cm^{-2} (PdRhMoFeMn HEMs), 0.027 mg cm^{-2} (RhMoFeMn metallenes), 0.039 mg cm^{-2} (RhMoFeMn metallenes), and 0.057 mg cm^{-2} (PdRh metallenes and Pt/C), electrolyte pH: 0.37 ± 0.05 (0.5 M H_2SO_4), 6.96 ± 0.03 (1 M PBS), and 13.81 ± 0.14 (1 M KOH), electrolyte resistance: 6.4 ± 0.3 Ω (0.5 M H_2SO_4), 21.6 ± 0.6 Ω (1 M PBS), and 5.5 ± 0.4 Ω (1 M KOH).

the type and concentration of metal precursors and reaction temperature, senary PdRhIrCoFeMo HEMs, septenary PdRhIrFeMoMnW HEMs, and octonary PdRhIrMnMoRuFeCo HEMs were successfully fabricated. TEM and AFM analyses confirm the metallene morphology and ultrathin structure of less than 1.5 nm (Supplementary Figs. 10 and 11). HRTEM images show that there was no formation of nanoparticles or clusters on the surfaces of senary, octonary, and septenary HEMs, proving that all metal atoms are well mixed within the metallenes. They also display clear lattice fringes with lattice distances of 0.227, 0.230, and 0.229 nm, corresponding to the {111} facets of senary, octonary, and septenary HEMs, respectively. From the STEM-EDS element mappings (Supplementary Fig. 10), SEM-EDS (Supplementary Fig. 12), and ICP-OES results (Supplementary Table 1), each element content of HEMs is in the range of 5–35% and distributed homogeneously around the HEMs without component segregation. In addition, the XRD pattern shows that all HEMs have an *fcc* alloy structure without phase separation. The broadening and weakening of their peaks and the shift of peak positions relative to pure Pd are due to the introduction of other metal elements, proving the successful formation of single-phase HEMs (Supplementary Fig. 13). Therefore, our synthetic strategy possesses general suitability for the manufacture of HEMs.

Electrocatalytic performance toward HER

To assess the potential electrocatalytic capabilities of as-prepared HEMs, the HER activity of sub-nanometric PdRhMoFeMn HEMs was first measured utilizing a standard three-electrode configuration in a 0.5 M H_2SO_4 aqueous solution. For comparison, the HER performance of PdMoFeMn (Supplementary Fig. 14), RhMoFeMn (Supplementary Fig. 15), and PdRh metallenes (Supplementary Fig. 16) synthesized by the same preparation method as PdRhMoFeMn HEMs, and Pt/C catalysts were also investigated as reference substances under the same electrochemical test conditions. All the polarization curves were calibrated against reversible hydrogen electrode (RHE) as shown in Supplementary Figs. 17 and 18. Figure 3a shows that PdRhMoFeMn HEMs have a near-zero onset potential (−0.16 mV) and only require a η_{10} of 6 mV, lower than those of RhMoFeMn metallenes (20 mV), PdRh metallenes (16 mV), and Pt/C (13 mV). However, the η_{10} of PdMoFeMn metallenes increases sharply to 57 mV, 51 mV higher than that of PdRhMoFeMn HEMs, indicating that Rh is the potential active site under acidic conditions. Impressively, PdRhMoFeMn HEMs produce an industrial-level current density (500 mA cm^{-2}) at a small overpotential of 46 mV, which is much better than reference samples (Supplementary Fig. 19). Moreover, the resulting Tafel slope of PdRhMoFeMn HEMs is 16 mV dec^{-1}, smaller than those of RhMoFeMn metallenes (30 mV dec^{-1}), PdMoFeMn metallenes (64 mV dec^{-1}), PdRh metallenes (32 mV dec^{-1}), and Pt/C (17 mV dec^{-1}) (Fig. 3b). This result reflects that the Rh introduction optimizes the electrochemical hydrogen adsorption/desorption and the HER pathway changes from the Volmer-Heyrovsky mechanism for PdMoFeMn metallenes to the Volmer-Tafel mechanism for PdRhMoFeMn HEMs[53,54]. Through extrapolating the Tafel plots, the exchange current density (j_0) of PdRhMoFeMn HEMs was determined (4.9 mA cm^{-2}). It is remarkably greater than that of RhMoFeMn metallenes (2.2 mA cm^{-2}), PdMoFeMn metallenes (1.2 mA cm^{-2}), PdRh metallenes (2.2 mA cm^{-2}), and Pt/C (1.8 mA cm^{-2}), suggesting the fastest kinetic essence towards hydrogen evolution (Supplementary Fig. 20). To fairly evaluate their potential for practical applications, the calculated mass activity of each sample was normalized with the loading of PGMs. Figure 3c shows that PdRhMoFeMn HEMs achieve the highest mass activity of 35.7 A per milligram PGMs at an overpotential of 50 mV, which is 16.2, 178.4,

37.5, and 9.1 times higher than those of RhMoFeMn metallenes, PdMoFeMn metallenes, PdRh metallenes, and Pt/C, respectively. As a key evaluation parameter for advanced electrocatalysts, the electrochemical durability of PdRhMoFeMn HEMs was further assessed in a 0.5 M H_2SO_4 electrolyte. As illustrated in Fig. 3d, the polarization curves of PdRhMoFeMn HEMs before and after 10,000 cyclic voltammetry (CV) cycles remain virtually unchanged, and the η_{100} of PdRhMoFeMn HEMs increases only 1 mV after 10,000 cycles. In striking contrast, the polarization curves of RhMoFeMn metallenes, PdMoFeMn metallenes, PdRh metallenes, and Pt/C have displayed visible deterioration after 10,000 cycles (Supplementary Fig. 21). Moreover, the chronopotentiometry curve in Fig. 3d shows that PdRhMoFeMn HEMs have only 3 mV degradation after 20 h, further proving its superior long-term stability. Besides, the TEM images show that PdRhMoFeMn HEMs maintain the nanosheet shape, and the distribution of the nanosheet is still uniform without aggregation (Supplementary Fig. 22a, b). XRD results in Supplementary Fig. 22c suggest that (111) facet-dominated *fcc* structure could be well retained after 10,000 cycles. Moreover, the ICP-OES characterizations before and after 10,000 cycles indicate that there was no obvious change in the composition of PdRhMoFeMn HEMs (Supplementary Fig. 22d). Supplementary Fig. 23 also shows that after 10,000 cycles, there are no significant changes observed in the XANES spectra of each element. However, some metallic Pd sites may appear (Supplementary Fig. 23a), with a relatively small impact on the performance of PdRhMoFeMn HEMs, which is proved by almost unchanged HER activity after 10,000 cycles (Fig. 3d).

Since proton or hydroxide concentration will always affect the performance of electrocatalysts during electrolysis, a hopeful electrocatalyst should function effectively at all pH. Therefore, the HER activities of PdRhMoFeMn HEMs were also examined under neutral and alkaline conditions. As shown in Fig. 3e and Supplementary Fig. 24, PdRhMoFeMn HEMs require the smallest η_{10} of 23 and 26 mV and the highest mass activities of 1.97 and 2.93 A per milligram PGMs at an overpotential of 100 mV in 1.0 M PBS and 1.0 M KOH, respectively, outperforming all control samples. Furthermore, the Tafel analysis was applied to insight into the HER kinetics of various catalysts in neutral and alkaline electrolytes (Fig. 3f). Under the neutral condition, the Tafel slopes of RhMoFeMn and PdMoFeMn metallenes are 75 and 96 mV dec^{-1}, respectively, whereas PdRh metallene shows a Tafel slope of 56 mV dec^{-1} (Supplementary Fig. 24b), indicating that the RDS for RhMoFeMn and PdMoFeMn metallenes is the Volmer step ($* + H_2O + e^- \rightarrow H^* + OH^-$), whereas the RDS for PdRh metallenes is the Heyrovsky step ($H^* + H_2O + e^- \rightarrow H_2 + OH^-$)[30]. It suggests that the coexistence of Pd and Rh is beneficial for the water dissociation reaction. The Tafel slope of PdRhMoFeMn HEMs further decreases to 33 mV dec^{-1}, demonstrating that the intervention of Mo, Fe, and Mn can alter the HER pathway from the Heyrovsky mechanism with electrochemical desorption as the RDS for PdRh metallenes to the Volmer-Tafel mechanism for PdRhMoFeMn HEMs with chemical desorption of hydrogen as the RDS[55]. In alkaline electrolytes, the Tafel slope of RhMoFeMn, PdMoFeMn, and PdRh metallenes are 85, 168, and 101 mV dec^{-1}, respectively, while PdRhMoFeMn HEMs demonstrate a Tafel slope of 41 mV dec^{-1}, indicating that the reaction HER pathways of all sample are the Volmer-Heyrovsky mechanism but only the RDS for PdRhMoFeMn HEMs is the Heyrovsky step (Supplementary Fig. 24e)[56]. It can be inferred that the Mo, Fe, and Mn atoms may have a strong adsorption capacity for hydroxide ions, thus accelerating the water dissociation step on the catalyst surface, similar to previous literature reports[57]. Meanwhile, PdRhMoFeMn HEMs show the greatest j_0 of 2.0 mA cm^{-2} in the neutral medium and 2.3 mA cm^{-2} in the alkaline medium, further proving its superior HER kinetics (Supplementary Fig. 25). As shown in Supplementary Figs. 26 and 27, the polarization curves of PdRhMoFeMn HEMs have a negligible negative shift after 10,000 cycles relative to those of RhMoFeMn metallenes, PdMoFeMn metallenes, PdRh metallenes, and Pt/C in 1.0 M PBS and 1.0 M KOH media, suggesting the excellent stability and durability under both neutral and alkaline conditions.

To investigate the reasons for the enhanced HER performance of PdRhMoFeMn HEMs, we analyzed the electrochemical double-layer capacitance (C_{dl}) by performing CV tests with different scan rates. Whereby, PdRhMoFeMn HEMs exhibit the C_{dl} values of 14.8, 14.6 and 19.0 mF cm^{-2}, superior to RhMoFeMn metallenes (12.6, 3.9, and 15.8 mF cm^{-2}), PdMoFeMn metallenes (4.4, 7.1 and 8.1 mF cm^{-2}), and PdRh metallenes (2.8, 6.4, and 6.2 mF cm^{-2}) in 0.5 M H_2SO_4, 1.0 M PBS, and 1.0 M KOH electrolytes, respectively, suggesting that PdRhMoFeMn HEMs possess more exposed electroactive sites for enhanced HER activity (Supplementary Fig. 28–30). Thereafter, the turnover frequency (TOF) was determined to quantify the electrocatalytic efficiency of each active site. As shown in Supplementary Fig. 31, PdRhMoFeMn HEMs have higher TOF values than other benchmarked electrocatalysts in the entire investigated potential range at all pH levels, indicating a prominent catalytic capacity for hydrogen production. Distinctly, PdRhMoFeMn HEMs deliver high TOF values of 19.40 $H_2\ s^{-1}$, which is about 16.58, 176.36, 27.32, and 4.92 times higher than those of RhMoFeMn metallenes (1.17 $H_2\ s^{-1}$), PdMoFeMn metallenes (0.11 $H_2\ s^{-1}$), PdRh metallenes (0.71 $H_2\ s^{-1}$) and Pt/C (3.94 $H_2\ s^{-1}$) at an overpotential of 50 mV in acidic media, respectively (Supplementary Fig. 31b). Moreover, PdRhMoFeMn HEMs also show considerably greater TOF values of 1.08 and 1.59 $H_2\ s^{-1}$ than all control catalysts at an overpotential of 100 mV in 1.0 M PBS and 1.0 M KOH, respectively (Supplementary Fig. 31d–f). Additionally, the HER performance of quinary PdRhMoFeMn HEMs was also compared with that of senary PdRhIrCoFeMo, septenary PdRhIrFeMoMnW, and octonary PdRhIrMnMoRuFeCo HEMs. As shown in Supplementary Fig. 32, PdRhMoFeMn HEMs exhibit smaller overpotential than senary, septenary, and octonary HEMs at the same current density under acidic, neutral, and alkaline environments. PdRhMoFeMn HEMs have larger C_{dl} values than senary, septenary, and octonary HEMs over a wide pH range, proving the higher atomic utilization efficiency of PdRhMoFeMn HEMs (Supplementary Figs. 33–35). Particularly, all these HEMs exhibit small negative shifts after 10,000 CV cycles, indicating their excellent electrochemical stability (Supplementary Fig. 36). The remarkable HER performance of PdRhMoFeMn HEMs outperforms other modern noble metal-based electrocatalysts over a broad pH range (Supplementary Fig. 37, Supplementary Table 2–4).

Theoretical simulations

To understand the synergistic mechanisms of multiple active sites on PdRhMoFeMn HEMs for the enhanced HER performance in the pH 0 to pH 14 range, the theoretical study was conducted for PdRh, PdMoFeMn, RhMoFeMn, and PdRhMoFeMn (Fig. 4a, Supplementary Figs. 38 and 39). As shown in Fig. 4b and Supplementary data 1, molecular dynamics simulations were first implemented to evaluate the thermal stability of PdRhMoFeMn HEMs under different temperatures (300 K, 400 K, and 500 K). The free energy of PdRhMoFeMn HEMs fluctuates in a narrow range with time evolution in all cases at 300, 400, and 500 K. This result indicates that the structure of PdRhMoFeMn HEMs is thermally stable, which is verified by the long-term electrochemical stability tests for HER. Supplementary Fig. 40 and Supplementary data 2 show that electrons are transferred from Fe, Mo, and Mn to Pd and Rh in HEMs due to the lower electronegativity of Fe, Mo, and Mn.

The Gibbs free energy of hydrogen adsorption (ΔG_{H^*}) is a common indicator to evaluate electrocatalysts' HER performance. Supplementary Fig. 41 shows the atomic configurations of different sites in PdRhMoFeMn HEMs during the H* adsorption process and the detailed calculation of ΔG_{H^*} for the above-mentioned sites was listed in Supplementary Table 5. Figure 4c reveals that the Rh top site has the lowest ΔG_{H^*} (−0.132 eV) relative to other comparison sites, indicating

https://doi.org/10.1038/s41467-024-54589-0

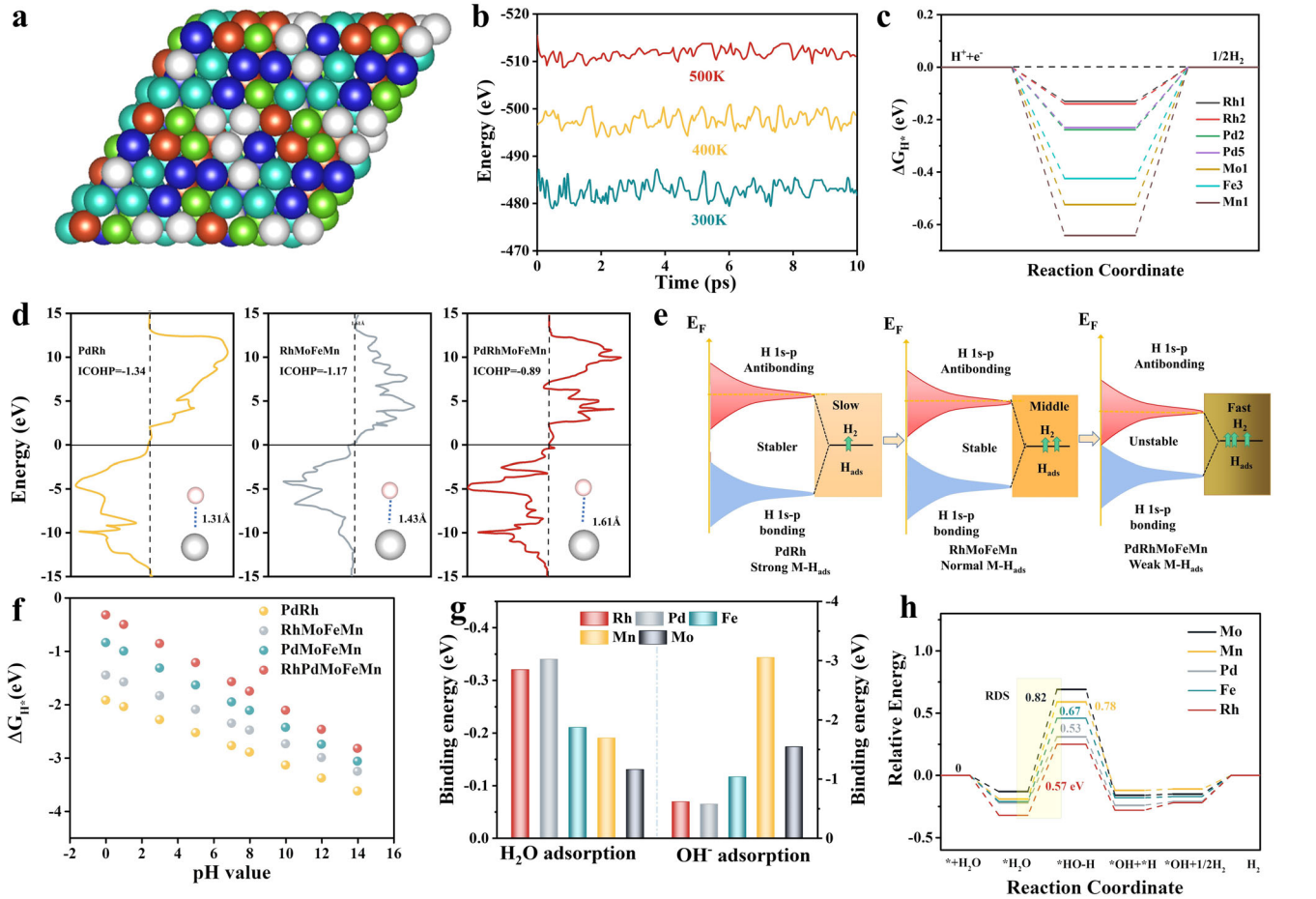

Fig. 4 | DFT calculations results. a The computational modeling of PdRhMoFeMn HEMs. **b** Molecular dynamics simulations of PdRhMoFeMn HEMs at 300, 400, and 500 K. **c** The ΔG_{H^*} profiles on various catalytic sites of PdRhMoFeMn HEMs. **d** The COHP calculations of RhMoFeMn metallenes, PdRh metallenes, and PdRhMoFeMn HEMs. **e** The Rh-H binding strength of RhMoFeMn metallenes, PdRh metallenes, and PdRhMoFeMn HEMs. **f** The ΔG_{H^*} of RhMoFeMn metallenes, PdRh metallenes, and PdRhMoFeMn HEMs at different pH values. **g** The adsorption energy of water and hydroxide at different sites for PdRhMoFeMn HEMs. **h** The reaction energy profile for water dissociation on various catalytic sites of PdRhMoFeMn HEMs.

that the Rh site has the best binding strength to hydrogen and serves as the main active ingredient to contribute to the excellent acidic HER performance. Subsequently, the ΔG_{H^*} of Rh sites in PdRh, PdMoFeMn, RhMoFeMn, and PdRhMoFeMn were also calculated (Supplementary Fig. 42). As displayed in Supplementary Fig. 43 and Supplementary Table 6, the ΔG_{H^*} of PdRhMoFeMn is −0.132 eV, which is significantly higher than that of PdRh (−0.528 eV) and RhMoFeMn (−0.465 eV). This indicates that the H* adsorption and desorption of PdRhMoFeMn are facilitated after the formation of high-entropy due to the weakened metal (Pd, Mo, Fe, Mn)-H_{ads} (M-H_{ads}) bonds. Such weakened M-H_{ads} bond can be further verified by the projected density of state (PDOS) and the crystal orbital Hamilton population (COHP) calculations. It can be found that the d-band center of Rh in PdRhMoFeMn (-1.95 eV) moves away from the Fermi level compared with those of Rh in PdRh (−1.43 eV) and RhMoFeMn (−1.68 eV) (Supplementary Fig. 44), revealing a weaker H* adsorption on the catalyst surface. Meanwhile, the integrated COHP (ICOHP) value for Rh in PdRhMoFeMn with H_2 (−0.89 eV) is higher than that of Rh in RhMoFeMn (−1.17 eV), and Rh in PdRh (−1.34 eV), suggesting the increased antibonding-orbital occupancy in the PdRhMoFeMn than those in PdRh and RhMoFeMn and the increased difficulty for the H_2 adsorption at Rh sites in PdRhMoFeMn (Fig. 4d). The increased antibonding-orbital occupancy can destabilize the H 1s-d antibonding, which leads to the further intensified desorption of Rh sites for hydrogen gas. Therefore, Rh in the PdRhMoFeMn electrocatalyst exhibits weaker M-H_{ads} bonds (with a longer bond length of 1.61 Å) than the PdRh catalyst (1.31 Å) and thus displays fast H_2 evolution (Fig. 4e). Specially, the Rh site in PdRhMoFeMn shows a ΔG_{H^*} that is closer to the optimal value (0 eV) compared with other sites and all control catalysts throughout the entire pH range, which agrees with the electrochemical measurement results (Fig. 4f and Supplementary Fig. 45).

The ΔG_{H^*} descriptor is not enough to fully reveal the HER performance of the catalyst under neutral and alkaline conditions due to the involvement of water adsorption and dissociation steps. Therefore, we systematically calculated the water adsorption and dissociation processes to uncover the origin of the superior performance of PdRhMoFeMn HEMs in neutral and alkaline electrolytes (Supplementary Fig. 46–49). Figure 4g shows that the Pd atom exhibits greater water adsorption energy than the rest of the four metal sites in PdRhMoFeMn HEMs. Likewise, the energy barrier required to break the H-OH bond is lowest on the Pd site as 0.53 eV relative to the Rh (0.57 eV), Mo (0.82 eV), Fe (0.67 eV), and Mn sites (0.78 eV) (Fig. 4h). The above analyses indicate that the H_2O adsorption and dissociation steps preferentially occur on the Pd site. Moreover, Fig. 4g and Supplementary Figs. 50 shows that the Mn atom has the highest binding energy to hydroxyl groups among the atoms in PdRhMoFeMn HEMs and the favorable OH desorption energy of PdRhMoFeMn at Mn sites is −0.85 eV, which can accelerate water dissociation into H and OH intermediates, followed by the reaction on the Rh site to produce H_2[57,58]. In addition, the Pd site in PdRhMoFeMn HEMs possesses the

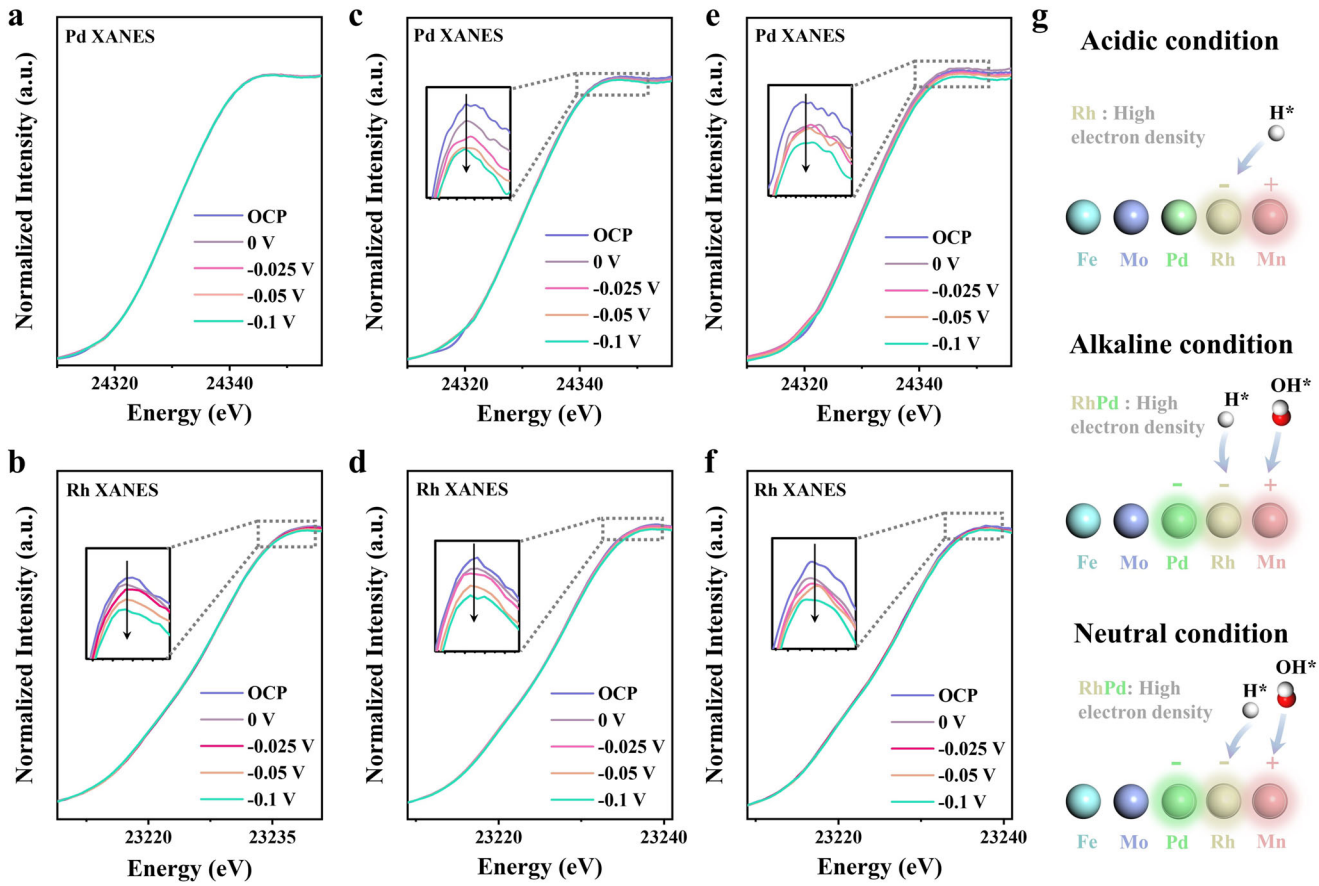

Fig. 5 | Operando XANES measurements of HER behaviors in various electrolytes. a, **b** Operando XANES spectra of Pd and Rh at various potentials in 0.5 M H_2SO_4. **c**, **d** Operando XANES spectra of Pd and Rh at studied potentials in 1.0 M KOH. **e**, **f** Operando XANES spectra of Pd and Rh at applied potentials in 1.0 M PBS. **g** Schematic illustration of the binding sites for H* and OH* in various electrolytes.

strongest adsorption capacity for water and requires the lowest water dissociation energy than PdRh, PdMoFeMn, and RhMoFeMn, highlighting the important role of high-entropy effects (Supplementary Figs. 51 and 52). Moreover, Fe and Mo have similar atomic radius to Pd, Rh, and Mn, which is more favorable for the formation of highly stable HEMs. Consequently, the high-entropy effects and the collaborative action of multiple active sites contribute to the improved water adsorption, the reduced water dissociation energy barrier, and the optimized formation and release behavior of H_2, which synergistically promote the HER performance of PdRhMoFeMn HEMs over a wide pH range.

Operando XAS study

To deeply shed light on the role of each active site and the corresponding catalytic reaction mechanism, the operando XAS measurements were performed on the PdRhMoFeMn HEM catalyst using a tailor-made cell in the three electrolytes representing universal pH (Supplementary Fig. 53). Supplementary Figs. 54–56 demonstrate the consistency of data processing and well-normalization across a wide range of XANES spectra. Under acidic conditions, the operando XANES spectrum of Pd sites in Fig. 5a shows the unchanged electron structure. In contrast, the decreasing white line intensity of Rh sites indicates high electronic density (Fig. 5b). These phenomena suggest that the electronic structure change of Rh sites can facilitate the interaction with the proton, thus promoting the kinetics during HER. The XANES spectra in Fig. 5c, d demonstrate a reduction in the white line intensity of both Pd and Rh, indicating an enhanced electron density on both Pd and Rh atoms upon the application of a reduction potential. This observation suggests that there is a charge transfer from other metal sites, which enhances the reactivity of the intermediate H* on the catalyst surface. Additionally, the operando XANES spectra of Mn show a decrease in electronic density, indicating a consistent result of charge transfer towards the Rh and Pd sites (Supplementary Figs. 57). In the neutral media, the Pd and Rh also exhibit the same catalytic behaviors compared with alkaline conditions, the increasing electronic density could facilitate the adsorption and desorption of intermediates (Fig. 5e, f). Figure 5g provides a detailed insight into the electronic structure of the HEM catalyst in different electrolytes under the catalytic process. Notably, the Pd site maintains the same electronic structure under acidic media. The increasing electron density of Pd sites in alkaline and neutral conditions accelerates the water dissociation process known as the Volmer step. Furthermore, Mn sites exhibit a decreased electronic density in each electrolyte, suggesting the charge redistribution in the HEM catalyst, which benefits the charge transfer towards other multi-metal sites (Supplementary Figs. 57). Noting that the high electron density of Rh under each electrolyte indicates that more charge transfer occurs at Rh sites, which are considered the primary reaction sites.

Operando EXAFS measurements were used to observe local geometry changes. As depicted in Fig. 6 and Supplementary Fig. 58, the Mn, Pd, and Rh sites exhibit distinct geometric structures, providing a clear insight into the detailed reaction mechanisms during the HER process. Specifically, for the Mn site, Mn-O remains nearly unchanged in acidic solutions (Supplementary Fig. 58a and Supplementary Table 7). An increase in Mn-O is observed only under alkaline and neutral conditions, suggesting the generation of more oxygen-related groups at the Mn sites (Supplementary Fig. 58b,c and Supplementary Tables 8 and 9). The EXAFS fitting of Mn also clearly demonstrates the

https://doi.org/10.1038/s41467-024-54589-0

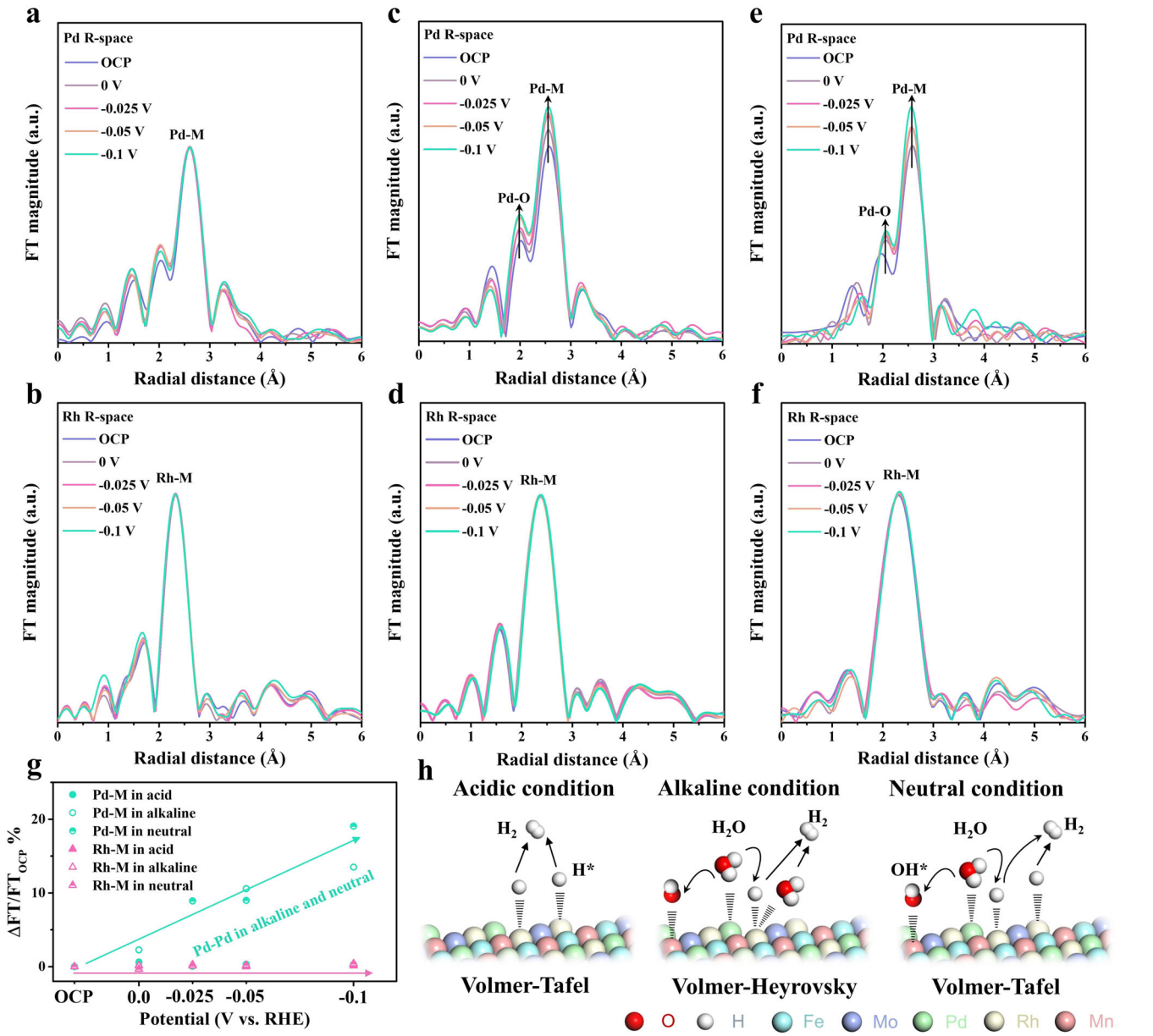

Fig. 6 | Operando EXAFS measurements of HER behaviors in various electrolytes. a, **b** Operando EXAFS spectra of Pd and Rh at different potentials in 0.5 M H_2SO_4 without phase correction. **c**, **d** Operando EXAFS spectra of Pd and Rh at varied potentials in 1.0 M KOH without phase correction. **e**, **f** Operando EXAFS spectra of Pd and Rh at applied potentials in 1.0 M PBS without phase correction. **g** The structural change of Pd-M and Rh-M in FT magnitude relative to the OCP state in various electrolytes. **h** Schematic illustration of multi-site synergistic mechanisms for HER in various electrolytes.

changes under different conditions (Supplementary Fig. 59). Figure 6a, b, and Supplementary Figs. 60a and 61a show that both Pd and Rh sites exhibit an unchanged geometric structure, suggesting a self-adaptive behavior in bonding with protons during the acidic HER. Supplementary Tables 10 and 11 further demonstrate the almost unchanged coordination environment of Pd and Rh. Notably, only Rh sites show a high electron density in XANES results, implying again that the Rh site serves as the main active center that interacts with protons in acidic media. In Fig. 6c, a slight increase in the Pd-O peak intensity is observed under alkaline conditions. EXAFS fitting further shows a clear trend of increased coordination numbers (Supplementary Fig. 60b and Supplementary Table 12), indicating some chemisorbed O on Pd sites. At the same time, the gradual increase in the coordination numbers of Pd-M implies the occurred structural reconstruction. Rh EXAFS results show that no obvious change in the coordination number of Rh-M was observed, suggesting that protons could easily react on electron-rich Rh sites in alkaline media (Fig. 6d, Supplementary Fig. 61b and Supplementary Table 13). In neutral electrolyte, similar phenomena as those under alkaline conditions were observed. The coordination numbers of Pd-O and Pd-M increase (Fig. 6e, Supplementary Fig. 60c and Supplementary Table 14) and the coordination environment of Rh-M is almost unchanged (Fig. 6f, Supplementary Fig. 61c and Supplementary Table 15). Furthermore, Fig. 6g clearly reflects the stable coordination environment of Rh-M. The increased coordination number of Pd-M in alkaline and neutral electrolytes implies local atomic rearrangement, which is beneficial for the activation of the catalyst and improves its HER kinetics. Simultaneously, based on Supplementary Fig. 62 k-space spectra, where a slight contribution from Pd-O is observed between 3–6 $Å^{-1}$, indicating the trend of chemisorbed oxygen species on Pd sites, and Pd-O fitting was also conducted to further understand the HER mechanisms. This result, combined with the above theoretical calculations and Tafel

slope analysis, suggests a possible water dissociation process on Pd sites. Therefore, chemisorbed oxygen-related species were observed in Pd, Rh, and Mn, but only Mn formed obvious oxides in the end. Importantly, the above-mentioned relevant characterizations after stability tests indicate that the formation of trace amounts of Mn-related oxides has little effect on the morphology, crystal structure, and electronic structure of HEMs. DFT calculations also show that the ΔG_{H^*}, OH* adsorption energy, and OH* desorption energy of Mn-O/PdRhMoFeMn HEMs is −0.13, −3.18, and −0.84 eV, respectively, which is close to that of PdRhMoFeMn HEMs (−0.132, −3.05, and −0.85 eV) (Supplementary Figs. 63–67). These results indicate that the formation of trace oxide clusters during the reaction has minimal impact on its HER performance, which is consistent with its excellent HER stability.

These results illustrate the HER mechanisms of PdRhMoFeMn HEMs under different conditions (Fig. 6h). In acidic electrolytes, two H* absorbed on the Rh sites with the high electron density as the primary active species combine to generate H_2 and release through the Vomer-Tafel mechanism. Under alkaline conditions, the HER on the HEM surface follows the Volmer-Heyrovsky mechanism. The adsorbed water molecule dissociates on the Pd site to generate intermediate H* and OH, and then the generated H* moves to the Rh site to combine with a proton in another water molecule in the electrolyte to form H_2. Simultaneously, the formed OH intermediates are absorbed onto the Mn sites, which can destabilize bonds in the water molecule and release more Pd sites to accelerate the water dissociation process[57]. Subsequently, the OH adsorbed on the Mn sites is desorbed into the electrolyte. The difference between the reaction mechanism in neutral electrolyte and alkaline is that two protons produced by the dissociation of water on the Pd site are respectively absorbed on the Rh site and coupled to form H_2 through the Vomer-Tafel path.

Discussion

In summary, highly curved and sub-nanometer-thick HEMs composed of up to eight metallic elements were synthesized by a general one-pot wet-chemical method. Theoretic calculations reveal that Rh sites with optimal ΔG_{H^*} in PdRhMoFeMn HEMs serve as the potential active center for the stepped-up coupling of H* to H_2, contributing to excellent acidic HER performance. Moreover, strong hydroxyl group adsorption at Mn sites is conducive to water dissociation at Pd sites during the critical Volmer step, thus changing the rate-determining steps and achieving rapid H_2 generation in neutral and alkaline solutions. More importantly, operando XAS verified the ability of HEMs to stabilize multiple intermediates at different active centers, and atomically observed the active sites of Pd, Rh, and Mn and the mechanisms of multi-site synergy in various electrolytes during the electrocatalytic HER processes. Benefiting from the characteristic high-entropy effect, ultra-high atomic utilization efficiency, and multi-site cooperative behavior, the PdRhMoFeMn HEMs show low η_{10} and small Tafel slopes (6 mV and 16 mV dec^{-1} in 0.5 M H_2SO_4 solution; 23 mV and 33 mV dec^{-1} in 1.0 M PBS solution; 26 mV and 41 mV dec^{-1} in 1.0 M KOH solution), outperforming most reported noble metal-based HER catalysts. This work sheds light on the relevance between specific active sites and reaction intermediates in-depth, guiding the rational design of a new generation of 2D HEA electrocatalysts with editable active sites beyond other energy conversion technologies.

Methods

Chemicals

Palladium(ii) acetylacetonate ($Pd(acac)_2$, 99%), hexarhodium hexadecacarbonyl ($Rh_6(CO)_{16}$, Rh 57–60%), dodecacarbonyltriiron ($Fe_3(CO)_{12}$, 96%), Manganese carbonyl ($Mn_2(CO)_{10}$, 98.0%), molybdenum hexacarbonyl ($Mo(CO)_6$, 98.0%), dodecacarbonyltetrairidium ($Ir_4(CO)_{12}$, 98%), octacarbonyldicobalt ($Co_2(CO)_8$, 98%), tungsten hexacarbonyl ($W(CO)_6$, 97%), triruthenium dodecacarbonyl ($Ru_3(CO)_{12}$, 99%), ascorbic acid (AA, 99%), cyclohexane (99.7%), oleylamine (OAm, 70%) and acetone (≥99.5%) were purchased from Sigma-Aldrich without further processing.

Fabrication of HEMs

In the synthesis of the representative sub-nanometric PdRhMoFeMn HEMs, 9.5 mg $Pd(acac)_2$, 5.5 mg $Rh_6(CO)_{16}$, 5.5 mg $Fe_3(CO)_{12}$, 5.0 mg $Mn_2(CO)_{10}$, 35 mg $Mo(CO)_6$ and 25 mg AA was ultrasonically dispersed in 6.0 mL OAm to form the precursor solution. Afterwards, an oil bath at 150 °C was used to heat the mixture for eight hours. The HEM product was collected after centrifugation and four washes with a mixed solution of cyclohexane, acetone, and ethanol. For the synthesis of RhMoFeMn, PdMoFeMn, and PdRh metallenes, all the conditions were the same as those of PdRhMoFeMn HEMs except for varying the kinds of metallic precursors.

The preparations of senary PdRhIrCoFeMo HEMs, septenary PdRhIrFeMoMnW HEMs, and octonary PdRhIrMnMoRuFeCo HEMs were similar to that of quinary PdRhMoFeMn HEMs, except that the reaction temperature was 160 °C and the content of each metal salt was different in the precursor solutions, which were summarized in the Supplementary Table 16.

Characterization

The TEM, HRTEM, HAADF-STEM, and EDS elemental mapping images of these as-prepared samples were obtained using an FEI Tecnai F20 transmission electron microscope with a 200 kV acceleration voltage. The HRSTEM images were acquired with JEOL JEM-ARM200F aberration-corrected transmission electron microscope. The Thermo Scientific K-Alpha spectrometer was used for XPS analyses. XRD patterns were studied using an X'Pert PRO MPD (D8) instrument. The composition of these synthesized samples was determined using ICP-OES (PerkinElmer ICP 2100). ATHENA was used to process the acquired EXAFS data. EXAFS fitting was performed using the ARTEMIS module of the Demeter software packages based on the reported literature[59], and the details are presented in the Supplementary Information.

Electrochemical measurements

All catalyst samples were synthesized by dispersing as-prepared nanoparticles onto Ketjen carbon. All catalysts had a metal load of 20%. In the case of preparing the carbon-supported PdRhMoFeMn HEA catalyst, 4 mg PdRhMoFeMn HEAs dissolved in 4 ml cyclohexane were mixed with 16 mg Ketjen carbon dissolved in 16 ml cyclohexane, followed by sonicating for 2 hours. After magnetically stirring overnight, the loaded sample obtained by centrifugation was redispersed in 20 mL acetic acid and heated at 70 °C for 120 min to clean the organic residues on the surface of PdRhMoFeMn HEAs. Then, the catalyst was obtained via centrifugation, followed by three washes with ethanol, and dried in a vacuum at 50 °C. The homogeneous catalyst ink was created by ultrasonically dispersing 4 mg of the above-obtained catalyst in 1 ml solution consisting of 290 µL ethanol, 690 µL water, and 20 mL 5 wt% Nafion under an ice-water bath. Subsequently, the working electrode was prepared by drop-casting 5 µL electrocatalyst suspension onto a glassy carbon electrode (GCE) (diameter: 3 mm, area: 0.07 cm^2) and subsequent air drying. Therefore, the loading of the catalyst is 0.286 mg cm^{-2}.

CHI 760E electrochemical workstation with a standard three-electrode system was applied to carry out all electrochemical tests. A GCE (diameter: 3 mm, area: 0.07 cm^2) with a surface-modified catalyst and a carbon rod (diameter: 6 mm) were the working and counter electrodes, respectively. An Ag/AgCl electrode (3 M KCl) was used as the reference electrode in 1.0 M PBS (100 mL), whereas that in 0.5 M H_2SO_4 (100 mL) and 1.0 M KOH (100 mL) was a Hg/HgO electrode. The determined practical electrolyte pH values are 0.37 ± 0.05 for a 0.5 M H_2SO_4 solution, 6.96 ± 0.03 for a 1 M PBS solution, and 13.81 ± 0.14 for a 1 M KOH solution. All electrolytes is freshly prepared and used. The

calibration of reference electrodes was included in Supplementary Information (Supplementary Fig. 17). To assess the HER performance of these samples, linear sweep voltammetry (LSV) was conducted with 100% iR-compensation at a sweep rate of 10 mV s^{-1} in N_2-saturated 0.5 M H_2SO_4, 1 M PBS, and 1 M KOH electrolyte, respectively (i was the real working current and R is the measured series resistance). LSV curve was recorded until three repeated curves were obtained to ensure the accuracy of the electrochemical tests. Meanwhile, the resistance for the iR-compensation was obtained at the open circuit potential of electrochemical cell. For stability measurements, a chronoamperometry method was performed in the 0.5 M H_2SO_4 electrolyte at 10 mA cm^{-2} for 20 h. CV curves were recorded with gradually increased scan rates from 20 to 100 mV s^{-1} to estimate the C_{dl} of the aforementioned samples. The TOF of various electrocatalysts was calculated following the equation[53,60].

$$\mathrm{TOF}(s^{-1}) = \frac{j \times S}{n \times F \times N}(s^{-1})$$

In the above formula, the following symbols are used: j, S, n, F, and N. The first three of these refer to the current density (A cm^{-2}), the geometric area of a GCE (0.07 cm^2), and the number of electrons that participated in the electrocatalytic reaction (2 for HER), respectively. The latter two symbols represent Faraday's constant (96485.3 C mol^{-1}) and the upper limit number of active sites on a GCE, respectively. In calculating the N value, all noble metal atoms present in each sample loaded on a GCE were denoted to be active ingredients. Consequently, the resulting TOF represents the lower limit value.

Operando quick-scanning X-ray absorption measurements

Operando quick-scanning XAS tests were performed in transmission mode at TPS BL-44A in the National Synchrotron Radiation Research Center (NSRRC). These measurements relied on an electron storage ring operating at 3.0 GeV and a current of 360 mA. The collection time for each spectrum was 3 minutes, during which a continuous potential was applied, decreasing from 0 to −0.1 V (relative to RHE) (i–t). In transmission mode, both the sample spectrum and the reference spectrum (metal foil corresponding to each element) were collected simultaneously to ensure energy calibration. This experiment utilized a three-electrode setup with a self-assembled cell, featuring a large 3 ×3 cm^2 window sealed with Kapton tape (Supplementary Fig. 53). A small stick with a circular hole (0.5 cm^2) was also sealed with Kapton tape to shorten the distance between the electrode and the window, allowing X-rays to pass through the window and the electrode/electrolyte interface. Platinum was chosen as the counter electrode, while an Ag/AgCl electrode served as the reference electrode, with electrolytes of 0.5 M H_2SO_4, 1.0 M PBS, and 1.0 M KOH. The measurement methods were consistent across different electrolytes. Regarding the working electrode preparation, the catalyst powder used was a PdRhMoFeMn HEMs. 10 mg of catalyst powder were dissolved in ethanol containing 50 µL of a 5% Nafion solution (Sigma-Aldrich). The dispersion was further improved through sonication for 20 minutes. Subsequently, the mixed solution was uniformly drop-coated onto a 1 × 0.5 cm^2 carbon cloth and allowed to dry to obtain the working electrode.

Computational details

All calculations were done using the VASP model based on the MedeA platform[61]. The generalized gradient approximation and Perdew-Burke-Ernzerhof method on the basis of DFT were employed to depict the electron wave functions with an energy cutoff of 450 eV. Gamma point geometry optimization was conducted till the maximum force on each atom was 0.01 eV $Å^{-1}$ and the delta energy between self-consistent field cycles was lower than 10^{-5} eV. The details of PdRhMoFeMn HEM building are included in Supplementary Information[62]. To precisely reflect the calculations, the DFT + U corrections for transition metal (Rh:2.0 eV, Pd: 2.0 eV, Fe: 2.5 eV, Mo: 3.5 eV, and Mn: 4.0 eV) were employed[63].

Data availability

Full data supporting the findings of this study are available within the article and its Supplementary Information. Additional data are available from the corresponding authors upon request. Source data are provided with this paper.

References

1. Prabhu, P. & Lee, J. M. Metallenes as functional materials in electrocatalysis. *Chem. Soc. Rev.* **50**, 6700–6719 (2021).
2. Liu, D. B. et al. Atomically dispersed platinum supported on curved carbon supports for efficient electrocatalytic hydrogen evolution. *Nat. Energy* **4**, 512–518 (2019).
3. Chen, J. Z. et al. Ag@MoS_2 core-shell heterostructure as SERS platform to reveal the hydrogen evolution active sites of single-layer MoS_2. *J. Am. Chem. Soc.* **142**, 7161–7167 (2020).
4. Do, V. H. et al. Surface activation of atomically thin metal nitride by confined nanoclusters to trigger pH-universal hydrogen evolution. *Joule* **7**, 2118–2134 (2023).
5. Deng, K. et al. Hydrogen spillover effect tuning the rate-determining step of hydrogen evolution over Pd/Ir heterometallene for industry-level current density. *Appl. Catal. B-Environ.* **352**, 124047 (2024).
6. Li, Y. H. et al. Interstitial boron-triggered electron-deficient Os aerogels for enhanced pH-universal hydrogen evolution. *Nat. Commun.* **13**, 1143 (2022).
7. Xiao, P. et al. Molybdenum phosphide as an efficient electrocatalyst for the hydrogen evolution reaction. *Energy Environ. Sci.* **7**, 2624–2629 (2014).
8. Sun, L. B., Reddu, V. & Wang, X. Multi-atom cluster catalysts for efficient electrocatalysis. *Chem. Soc. Rev.* **51**, 8923–8956 (2022).
9. Li, Y. H., Kidkhunthod, P., Zhou, Y. T., Wang, X. & Lee, J. M. Dense heterointerfaces and unsaturated coordination synergistically accelerate electrocatalysis in Pt/Pt_5P_2 porous nanocages. *Adv. Funct. Mater.* **32**, 2205985 (2022).
10. Zhu, J., Hu, L. S., Zhao, P. X., Lee, L. Y. S. & Wong, K. Y. Recent advances in electrocatalytic hydrogen evolution using nanoparticles. *Chem. Rev.* **120**, 851–918 (2020).
11. Do, V. H. et al. Surface confinement of atomically thin Pt nanoclusters on 2D δ-MoN for durable pH-universal hydrogen evolution. *Adv. Funct. Mater.* **33**, 2302297 (2023).
12. Li, H. D., Lai, J. P., Li, Z. J. & Wang, L. Multi-sites electrocatalysis in high-entropy alloys. *Adv. Funct. Mater.* **31**, 2106715 (2021).
13. Yang, B. B. et al. High-entropy enhanced capacitive energy storage. *Nat. Mater.* **21**, 1074–1080 (2022).
14. George, E. P., Raabe, D. & Ritchie, R. O. High-entropy alloys. *Nat. Rev. Mater.* **4**, 515–534 (2019).
15. Kwon, J. et al. Tailored electronic structure of Ir in high entropy alloy for highly active and durable bifunctional electrocatalyst for water splitting under an acidic environment. *Adv. Mater.* **35**, 2300091 (2023).
16. Li, H. D. et al. Fast site-to-site electron transfer of high-entropy alloy nanocatalyst driving redox electrocatalysis. *Nat. Commun.* **11**, 5437 (2020).
17. Zhang, H. W., Jin, X. D., Lee, J. M. & Wang, X. Tailoring of active sites from single to dual atom sites for highly efficient electrocatalysis. *ACS Nano* **16**, 17572–17592 (2022).
18. Lei, X. et al. High-entropy single-atom activated carbon catalysts for sustainable oxygen electrocatalysis. *Nat. Sustain.* **6**, 816–826 (2023).
19. Rao, P. et al. Movable type printing method to synthesize high-entropy single-atom catalysts. *Nat. Commun.* **13**, 5071 (2022).

20. Li, X. G. et al. Molecule confined isolated metal sites enable the electrocatalytic synthesis of hydrogen peroxide. *Adv. Mater.* **34**, 2104891 (2022).
21. Xie, S. H. et al. Pt atomic single-layer catalyst embedded in defect-enriched ceria for efficient CO oxidation. *J. Am. Chem. Soc.* **144**, 21255–21266 (2022).
22. Lu, Q. C. & Wang, X. Recent progress of sub-nanometric materials in photothermal energy conversion. *Adv. Sci.* **9**, 2104225 (2022).
23. Takimoto, D. et al. Platinum nanosheets synthesized via topotactic reduction of single-layer platinum oxide nanosheets for electrocatalysis. *Nat. Commun.* **14**, 19 (2023).
24. Deng, K. et al. Lattice strain and charge redistribution of Pt cluster/Ir metallene heterostructure for ethylene glycol to glycolic acid conversion coupled with hydrogen production. *Small* **20**, 2305000 (2024).
25. He, Y. M. et al. Amorphizing noble metal chalcogenide catalysts at the single-layer limit towards hydrogen production. *Nat. Catal.* **5**, 212–221 (2022).
26. Luo, M. C. et al. PdMo bimetallene for oxygen reduction catalysis. *Nature* **574**, 81–85 (2019).
27. Jose, V. et al. Activating amorphous Ru metallenes through Co integration for enhanced water electrolysis. *Adv. Energy Mater.* **13**, 2301119 (2023).
28. Sun, Y. F. & Dai, S. High-entropy materials for catalysis: a new frontier. *Sci. Adv.* **7**, eabg1600 (2021).
29. Zhao, Y. G. et al. Oxygen evolution/reduction reaction catalysts: from in situ monitoring and reaction mechanisms to rational design. *Chem. Rev.* **123**, 6257–6358 (2023).
30. Chen, J. D. et al. Reversible hydrogen spillover in Ru-WO_{3-x} enhances hydrogen evolution activity in neutral pH water splitting. *Nat. Commun.* **13**, 5382 (2022).
31. Wang, Y. H. et al. In situ Raman spectroscopy reveals the structure and dissociation of interfacial water. *Nature* **600**, 81–85 (2021).
32. Dong, J. C. et al. In situ Raman spectroscopic evidence for oxygen reduction reaction intermediates at platinum single-crystal surfaces. *Nat. Energy* **4**, 60–67 (2019).
33. Peng, C. K. et al. Zhang-Rice singlets state formed by two-step oxidation for triggering water oxidation under operando conditions. *Nat. Commun.* **14**, 529 (2023).
34. Cao, L. L. et al. Identification of single-atom active sites in carbon-based cobalt catalysts during electrocatalytic hydrogen evolution. *Nat. Catal.* **2**, 134–141 (2019).
35. Ding, J. et al. Circumventing CO_2 reduction scaling relations over the heteronuclear diatomic catalytic pair. *J. Am. Chem. Soc.* **145**, 11829–11836 (2023).
36. Deng, Y. C. et al. Operando spectroscopic analysis of axial oxygen-coordinated single-Sn-atom sites for electrochemical CO_2 reduction. *J. Am. Chem. Soc.* **145**, 7242–7251 (2023).
37. Tian, X. et al. Engineering bunched Pt-Ni alloy nanocages for efficient oxygen reduction in practical fuel cells. *Science* **366**, 850–856 (2019).
38. Ren, B. et al. Nano-crumples induced Sn-Bi bimetallic interface pattern with moderate electron bank for highly efficient CO_2 electroreduction. *Nat. Commun.* **13**, 2486 (2022).
39. Yao, Y. G. et al. High-entropy nanoparticles: Synthesis-structure-property relationships and data-driven discovery. *Science* **376**, eabn3103 (2022).
40. Lv, F. et al. A highly efficient atomically thin curved PdIr bimetallene electrocatalyst. *Natl Sci. Rev.* **8**, nwab019 (2021).
41. Zhang, J. et al. Cr-doped Pd metallene endows a practical formaldehyde sensor new limit and high selectivity. *Adv. Mater.* **34**, 2105276 (2022).
42. Hao, J. et al. Unraveling the electronegativity-dominated intermediate adsorption on high-entropy alloy electrocatalysts. *Nat. Commun.* **13**, 2662 (2022).
43. Feng, G. et al. Sub-2 nm ultrasmall high-entropy alloy nanoparticles for extremely superior electrocatalytic hydrogen evolution. *J. Am. Chem. Soc.* **143**, 17117–17127 (2021).
44. Peng, O. W. et al. Swinging hydrogen evolution to nitrate reduction activity in molybdenum carbide by ruthenium doping. *ACS Catal.* **12**, 15045–15055 (2022).
45. Song, J. T. et al. Promoting dinuclear-type catalysis in Cu_1-C_3N_4 single-atom catalysts. *Adv. Mater.* **34**, 2204638 (2022).
46. Chen, Z. X. et al. Addressing the quantitative conversion bottleneck in single-atom catalysis. *Nat. Commun.* **13**, 2807 (2022).
47. Do, V. H. et al. Pd-PdO nanodomains on amorphous Ru metallene oxide for high-performance multifunctional electrocatalysis. *Adv. Mater.* **35**, 2208860 (2023).
48. Yu, H. J. et al. Defect-rich porous palladium metallene for enhanced alkaline oxygen reduction electrocatalysis. *Angew. Chem. Int. Ed.* **60**, 12027–12031 (2021).
49. Prabhu, P. et al. Oxygen-bridged stabilization of single atomic W on Rh metallenes for robust and efficient pH-universal hydrogen evolution. *ACS Nano* **17**, 10733–10747 (2023).
50. Huang, S. et al. Sublayer stable Fe dopant in porous Pd metallene boosts oxygen reduction reaction. *ACS Nano* **16**, 522–532 (2022).
51. Chen, Z. W. et al. Unusual Sabatier principle on high entropy alloy catalysts for hydrogen evolution reactions. *Nat. Commun.* **15**, 359 (2024).
52. Feng, G. et al. Constructing fully-active and ultra-active sites in high-entropy alloy nanoclusters for hydrazine oxidation-assisted electrolytic hydrogen production. *Adv. Mater.* **36**, 2309715 (2024).
53. Tiwari, J. N. et al. Multicomponent electrocatalyst with ultralow Pt loading and high hydrogen evolution activity. *Nat. Energy* **3**, 773–782 (2018).
54. Zhang, H. B. et al. Dynamic traction of lattice-confined platinum atoms into mesoporous carbon matrix for hydrogen evolution reaction. *Sci. Adv.* **4**, eaao6657 (2018).
55. Jiao, Y., Zheng, Y., Davey, K. & Qiao, S. Z. Activity origin and catalyst design principles for electrocatalytic hydrogen evolution on heteroatom-doped graphene. *Nat. Energy* **1**, 16130 (2016).
56. Liu, K. et al. Coherent hexagonal platinum skin on nickel nanocrystals for enhanced hydrogen evolution activity. *Nat. Commun.* **14**, 2424 (2023).
57. Dinh, C. T. et al. Multi-site electrocatalysts for hydrogen evolution in neutral media by destabilization of water molecules. *Nat. Energy* **4**, 107–114 (2019).
58. Zhang, J. et al. OH spectator at IrMo intermetallic narrowing activity gap between alkaline and acidic hydrogen evolution reaction. *Nat. Commun.* **13**, 5497 (2022).
59. Ravel, B. & Newville, M. ATHENA, ARTEMIS, HEPHAESTUS: data analysis for X-ray absorption spectroscopy using IFEFFIT. *J. Synchrotron Radiat.* **12**, 537–541 (2005).
60. Xue, Y. et al. Anchoring zero valence single atoms of nickel and iron on graphdiyne for hydrogen evolution. *Nat. Commun.* **9**, 1460 (2018).
61. Kresse, G. & Furthmuller, J. Efficient iterative schemes for ab initio total-energy calculations using a plane-wave basis set. *Phys. Rev. B* **54**, 11169–11186 (1996).
62. He, R. et al. A 3d-4d-5d high entropy alloy as a bifunctional oxygen catalyst for robust aqueous zinc-air batteries. *Adv. Mater.* **35**, 2303719 (2023).
63. Zhao, X. et al. Electron modulation and morphology engineering jointly accelerate oxygen reaction to enhance Zn-air battery performance. *Adv. Sci.* **10**, 2205889 (2023).

Acknowledgements

This work was supported by the AcRF Tier 1 (grant RG105/19 and RG63/21) provided by Ministry of Education in Singapore, Foundation of State Key Laboratory of High-efficiency Utilization of Coal and Green Chemical

Engineering (Grant No. 2022-K31), National Science and Technology Council in Taiwan (grants NSTC 112-2112-M-213-022 and 112-2221-E-213-002-MY2) and National Synchrotron Radiation Research Center in Taiwan.

Author contributions

J.-M.L., Y.-G.L., and Y.L. conceived and designed the project. Y.L. was responsible for the synthesis, physical characterization, electrochemical measurements, and analysis of the overall experimental data. Y.S. and S.L.D.N. assisted in the processing and analysis of the data. Y.Z. performed and analyzed the theoretical calculations. Y.L. assisted in processing and analyzing the computational details. C.-K.P., Y.-C.C., S.-Y.C., and Y.-G.L. supported the operando and hard XAS experiments. C.-K.P. and Y.-G.L. participated in the operando XAS experiments and data analysis. Y.L. and C.-K.P. were responsible for integrating and writing the manuscript. J.-M.L. and Y.-G.L. were responsible for project management. All authors contributed to writing the manuscript.

Competing interests

The authors declare no competing interests.

Additional information

Supplementary information The online version contains supplementary material available at https://doi.org/10.1038/s41467-024-54589-0.

Correspondence and requests for materials should be addressed to Yuntong Sun, Yingtang Zhou, Yan-Gu Lin or Jong-Min Lee.

Peer review information *Nature Communications* thanks Boyang Li, and the other, anonymous, reviewers for their contribution to the peer review of this work. A peer review file is available.